Spark plasma sintering studies of nanosize lanthanide-doped ceria obtained by sol-gel method

C. PLAPCIANU[a*], C. VALSANGIACOM[a], JEREMY E. SCHAFFER[b], A.WIEG[c], J. GARAY[c], L. STANCIU[b,d]
[a]*NIMP, Department of Solid State Magnetism and Superconductivity, Bucharest-Magurele, Romania,*
[b]*Purdue University, School of Biomedical Engineering, West Lafayette, IN, USA,*
[c]*University of California Riverside, Riverside, CA, USA,*
[d]*Purdue University, School of Materials Engineering, West Lafayette, IN, USA*

Doped ceria powders, $Ce_{0.8}$ $Ln_{0.2}O_{2-x}$ (Ln = Gd^{3+}, Sm^{3+} and Yb^{3+}) were sintered to nearly full density by Spark Plasma Sintering at 1100 and 1200ºC. The starting powders were obtained via a sol-gel method and had nanometric dimensions: 26.4 nm (Gd), 19.3 nm (Sm) and 31.4 nm (Yb). Samples characterization was performed by SEM, TEM and XRD to determine their structural and microstructural characteristics. The ionic conductivities of the sintered samples were determined by impedance measurements. The influence of the chemical composition, sintering temperature and microstructural characteristics on the total ionic conductivity were evaluated and discussed.

(Received May 5, 2011; accepted September 15, 2011)

Keywords: Lanthamide doped Ceria, Spark plasma sintering sol-gel method

1. Introduction

Cerium oxides are well known as catalysts for reforming hydrocarbons, partial oxidation of methane in solid-oxide fuel cells (SOFCs) and for the direct production of hydrogen via the water-gas-shift reaction as mentioned by many research works. The use of ceria-based materials for this kind of applications is mainly based on the ease of Ce(III) generation from Ce(IV), i.e. CeO_2 is reduced at high temperature and low oxygen partial pressure, resulting in oxygen deficiency and partial electronic conductivity, which is advantageous for charge transport in SOFC electrode structure. This property can be amplified if ceria-based materials present themselves in nanostructure form with increased oxygen-ion conductivity and provides the possibility of producing solid electrolyte in solid fuel cells able to operate at low temperatures then the conventional doped-zirconia based SOFC ones require (above 800^0C), leading to material degradation [1-3]. Several studies have been conducted in an attempt to reduce the operation temperature of SOFCs [4, 5]. Ceria (CeO_2) has unique catalytic, electrochemical and storage characteristics that makes it attractive for a large array of applications, such as catalysts, solid oxide fuel cell systems, and gas sensors. Moreover, doping with rare earth elements leads to materials with superior chemical and physical stability, high oxygen mobility and high concentration of oxygen vacancies [6, 7]. For example, when doped with elements such as Gd (GDC), Yb (YDC) or Sm (SDC), ceria displays ionic conductivity superior to zirconia, making it an attractive alternative for medium-temperature applications in solid-state electrochemical devices [7-9]. Another advantage of cerium oxide over zirconium oxide lies in the fact that ceria's fluorite structure does not change upon doping [10-16]. Bulk nanostructured yttria-stabilized zirconia (YSZ) and Sm-doped ceria have been investigated as alternative materials for devices operating at medium or low temperatures [3,5]. For SOFC applications, the electrolyte has to meet gas tight requirements, and therefore a high density is required. Kim et al. recently reported that low temperature operation of SOFCs has been achieved only for *nanostructured* bulk materials [17]. Nanostructured bulk cerium oxide has only recently been investigated by two research groups [17-19]. Most of the studies on cerium oxide materials involved either mostly a very low dopant level or only considered one type of dopant [19]. Spark Plasma Sintering (SPS) is a consolidation technique that uses a combination of pulsed electrical field application with high heating rates, to densify a large variety of powder materials that were proved to be difficult to sinter by other methods, while preserving a ultra-fine grain size [25, 26]. The electric field has an activating effect on mechanisms that dominate each stage of the process (surface activation by the pulsed current, acceleration of diffusion kinetics) resulting in enhanced densification and increase of the rate of sintering neck growth [29-31]. A possible explanation for this are effects such as localized overheating at particle contacts and the cleaning of particles surface through electrical discharges at the contacts. SPS is also a sintering process that applies a rapid heating rate and is completed in minutes compared to a few hours usually required for conventional sintering techniques. The present work report on the synthesis of ceria-doped powders by sol-gel technique and spark plasma sintering (SPS) of bulk nanostructured ceria doped with three different rare-earth metals (M=Yb^{3+}, Gd^{3+} and

Sm^{3+}) with doping levels of 20 wt%, and investigated the effect of the type of doping on their properties.

2. Experimental procedure

2.1 Synthesis of Precursor Powders

The precursor rare-earth doped cerium oxide powders can be synthesized by various techniques such as conventional powder mixing [20, 21], co-precipitation [22], sol-gel [23] and hydrothermal recrystallization [24]. The advantage of solution techniques over conventional techniques include the higher reactivity of the precursors and mixing at the molecular level, which leads to better sintering at lower temperatures. In this work, the high purity cerium hexahydrate $Ce(NO_3)_3{\cdot}6H_2O$ (99.99% Sigma Aldrich), gadolinium hexahydrate $Gd(NO_3)_3{\cdot}6H_2O$ (99.99% Sigma Aldrich), ytterbium pentahydrate $Yb(NO_3)_3{\cdot}5H_2O$ (99.99% Sigma Aldrich) and samarium hexahydrate $Sm(NO_3)_3{\cdot}6H_2O$ (99.99% Sigma Aldrich) were used as starting materials. Other reagents were ammonium carbonate $(NH_4)_2CO_3$ (99.999% Sigma Aldrich) and oxalic acid (99.5% Sigma Aldrich).

All nitrates were slowly dissolved in deionised water, and the stock solutions of 0.4 M of $Yb(NO_3)_3$, $Sm(NO_3)_3$ and $Gd(NO_3)_3$ were prepared. The rare earth metal nitrate solution was mixed with 2 times quantiy of stock solution of 0.8 M of $Ce(NO_3)_3$, keeping a molar ratio Ce:M = 4:1 (M = Yb, Sm and/or Gd). The solutions were magnetically stirred for 40 min. at room temperature for homogenization. Then, a calculated quantity of $(NH_4)_2CO_3$ 10 wt% solution was added as precipitation agent, followed by a solution of oxalic acid in the molar ratio OX:M = 1:2 (OX - oxalic acid, M – all metals). After OX addition, the solution was heated at 70 ^{0}C under continuous stirring, until a yellow gel was formed, which was then dried in an oven for about 2 hours at 100^{0}C, and then grinded in a porcelain mortar. All the powders were then heated for 1 hour at 600 ^{0}C, and characterized by TG-DTA and XRD to determine thermal behavior and phase composition.

2.2 Spark Plasma Sintering

The powders were densified by SPS. The SPS densification experiments were performed with a laboratory apparatus capable of delivering 4800 A and 150 kN load. In our system the load is delivered by a Universal test frame (Instron 5584, Instron Inc, USA) and the current is provided by programmable power supplies (Xantrex Inc, Canada). All experiments were performed using DC current. The experiments were performed under vacuum ($< 4 \times 10^{-4}$ Torr), in a custom fabricated water-cooled high vacuum chamber (MDC Corp., USA). All experiments were performed under high vacuum ($\leq 4.2 \times 10^{-4}$ Torr). Temperature control is accomplished through feed back from a thermocouple (grounded and sheathed type–N, diameters 0.10 mm with sheath diameter 0.50 mm). The thermocouples are inserted in holes drilled in the graphite die at a point halfway between the outer and inner diameter of the die. The powder was placed in the dies and pre-pressed to 70 MPa at room temperature. Subsequently, the temperature was raised to 1100 °C (or 1200 °C) with a heating rate of ~200 °C min^{-1}. The holding time at 1100°C and/or 1200 °C was 1 min. The resulted samples were characterized by SEM and EIS.

2.3 Samples Characterization

The microstructure of both precursor powders and SPS sintered samples was investigated by TEM using a JEOL 2000EX microscope operating at 200 kV. The XRD spectra were recorded with a Bruker D8 Advance Powder Diffractometer (Cu K_α radiation) in the range $2\theta = 20 – 90^0$. The SEM imaging was performed on fractured samples using a FEI Nova 200 FEG after 120 s of palladium physical vapor deposition to prevent charging.

A Solartron potentiostat (model 1252A) and frequency analyzer (model 1287A) were used in 2-channel mode to generate and measure the impedance response of each material. Scanning was performed under voltage control at 50 mV amplitude with zero nominal DC offset over the frequency range from 300 kHz to 0.1 Hz. Silver mesh current collectors (Alfa Aesar 40935) were attached to each material using adhesive silver paste (Alfa Aesar 44075). The contact analysis area was nominally 20 mm^2. Prior to analysis, each electrode assembly was fired at 450 ^{o}C for 8 hours. Impedance spectroscopy was run in air at temperatures ranging from 220 ^{o}C to 450 ^{o}C. The actual sample temperature was monitored using a thermocouple (Omega, type K, ungrounded probe) that was placed adjacent to the cell within the 75 mm diameter ceramic furnace tube (Lindberg, a division of Thermal Product Solutions, USA). The ends of the furnace tube were muffled with glass fiber to reduce forced convection at the cell. A four element equivalent circuit model (inset Figure 6a) was fit to the resultant impedance spectra using the complex non-linear fitting procedure built into Zview software (V2.6, Scribner Associates, Inc.) with Calc-Modulus weighting.

3. Results and discussion

The thermogravimetric analysis of as synthesis ceria doped precursors revealed the loss of physiosorbed and structural water as well as decomposition and of organic byproducts of the initial synthesis (figure 1). Ceria doped dried gel exhibits a 3 step mass decrease corresponding to water elimination of about 1%, (first small endothermic peak at 100^{0}C), followed by $Ce_{0.8}Ln_{0.2}(OH)CO_3$ hydroxycarbonate decomposition (second small endothermic peak at 160^{0}C) and oxalic acid elimination marked by the big sharp endothermic peak at 200^{0}C, representing about 14% . The total weight loss is around 15% for all ceria doped precursor powders. The exothermic peak at 380^{0}C can be assigned to oxide formation and crystallization taking part when rising the temperature over 400^{0}C, with no further mass loss for all samples no mater the doping element.

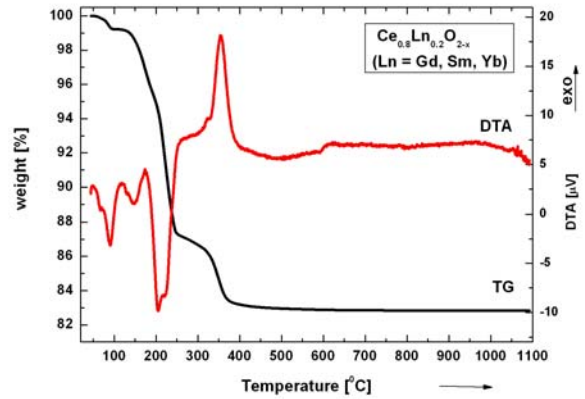

Fig. 1. Thermal behavior of ceria doped dried gels obtained via sol-gel synthesis. TG-DTA data for ceria doped oxide precursors are taken in flowing dry air at a heating rate of 10^0C/min

The XRD spectra for all the M^{3+}/CeO_2 precursor powders are shown in figure 2. All peaks in the XRD spectra were coordinated to standard cubic CeO_2 with slight shifts and had no other peaks, which indicate that the rare earth metal ions doped the CeO_2 crystal lattice. The peaks of Sm^{3+} doped CeO_2 and Gd^{3+} doped CeO_2 moved to lower 2θ values, due to the fact that the radii of Sm^{3+}(0.109 nm) and Gd^{3+}(0.105 nm) are larger than the radius of Ce^{4+}(0.097 nm) cation. When Ce^{4+} cations were replaced with nearly the same radius cations Yb^{3+} (0.098 nm) the interplanar spacing did not change, but peaks shifted toward higher 2θ values only due to distortion of lattice as the result of oxygen vacancy created when a trivalent cation is introduced into the lattice. Particle size analysis from TEM indicated that Yb^{3+} doping resulted into a notable smaller particle size than in the case of Gd^{3+} and Sm^{3+} doping. Compared to Gd^{3+} and Sm^{3+}, which present octahedral coordination, the same as Ce^{4+}, while the smaller Yb^{3+} cations prefer hexagonal coordination. Therefore the lattice distortion strength after doping is the largest in ytterbium doped ceria, which results in preventing particle growth.

The TEM measurements performed on $Ln_{0.2}Ce_{0.8}O_{2-x}$ powders (figure 3) revealed that particles have the same regular cubic shape. The morphology of the powders indicates the tendency towards aggregation and particle sizes in the nanometer range. Ytterbium-doped ceria displays the smallest average powder particle size, of 19.3 nm, while the gadolinium and samarium doped ceria have an average particle size of 31.4 and 26.4 nm, respectively (see Table 1).

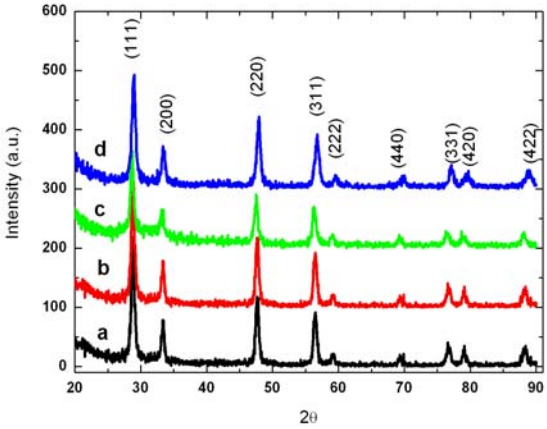

Fig. 2. X-ray patterns for Ceria doped oxide powders synthesized by sol-gel and calcined at 600 °C for 1 hour: a- undoped CeO_2; b- $Ce_{0.8}Sm_{02.}O_2$; $Ce_{0.8}Gd_{02.}O_2$; $Ce_{0.8}Yb_{02.}O_2$.

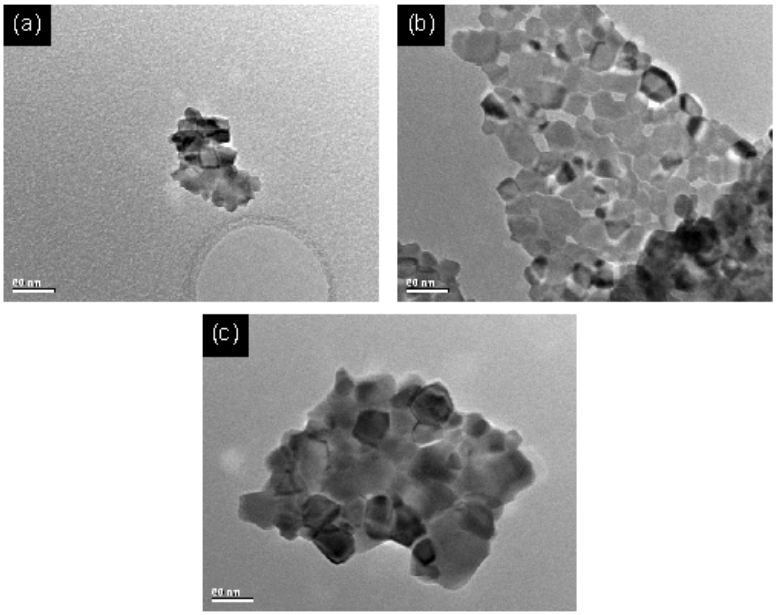

Fig. 3. TEM images of $M_{0.2}Ce_{0.8}O_{2-x}$ powders. (a) M = Yb; (b) M = Sm (c) M = Gd after heated at 600 °C.

Fully dense bulk samples were obtained by SPS sintering at 1100°C and/or 1200°C for one minute all samples. The technique uses a pulsed electric field application together with high heating rates and moderate pressures to sinter a large variety of powder materials, both conductive and non-conductive [25,26].

Figure 4 shows the SEM images of fractured $M_{0.2}Ce_{0.8}O_{2-x}$ samples, which were obtained by SPS sintering at 1100 ^{o}C. The images show that samples have homogenous microstructures, and indicate some degree of grain growth during sintering. Although completely avoiding grain growth during sintering, the high heating rate during SPS is beneficial in restraining it. This is due to the much shorter time that the samples are exposed to the temperatures in the initial stage of sintering, where grain coarsening mechanisms such as surface diffusion and evaporation condensation are dominant, as compared to conventional sintering. Grain size analysis of the experimental data showed that the average grain size of Sm^{3+} doped CeO_2 grains was 80 nm from original while the average grain sizes of Yb^{3+} and Gd^{3+} doped CeO_2 were 94 nm and 160 nm, respectively (Fig. 3).

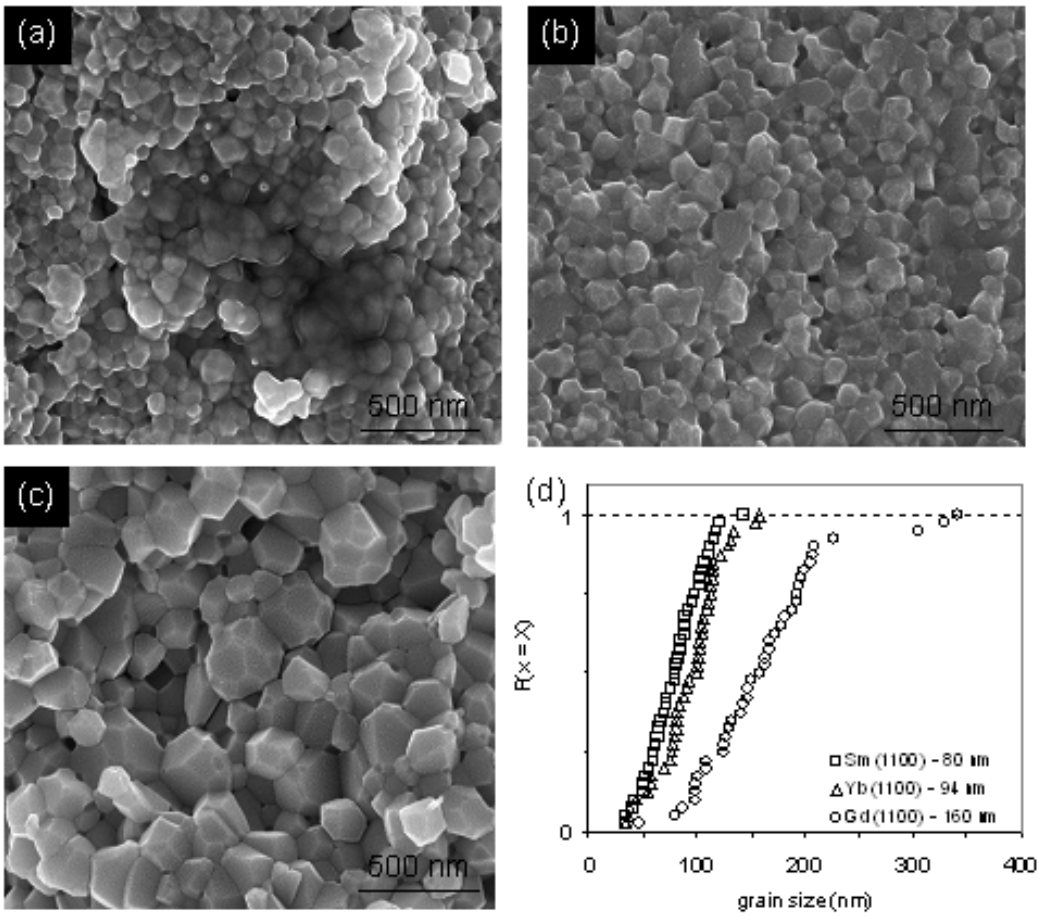

Fig. 4. SEM images of fractured $M_{0.2}Ce_{0.8}O_{2-x}$ samples, SPS sintered at 1100 ℃. (a) M = Sm^{3+}; (b) M = Yb^{3+}; (c) M = Gd^{3+}. (d) Empirical cumulative distribution plots of grain size showing mean grain sizes.

Figs. 5, 6 and 7 show a collection of TEM images of all SPS sintered samples. Bright field (BF) images were captured with the TEM, along with axial dark field (DF) images corresponding to all metal ions doped CeO_2 samples. In the TEM, the nearly complete powder densification is evident in the dark field images which show low compact porosity. TEM examination showed no segregation of metal oxide or formation of any secondary phase in these bulk samples, whatever the sintering temperature and the metal doping was.

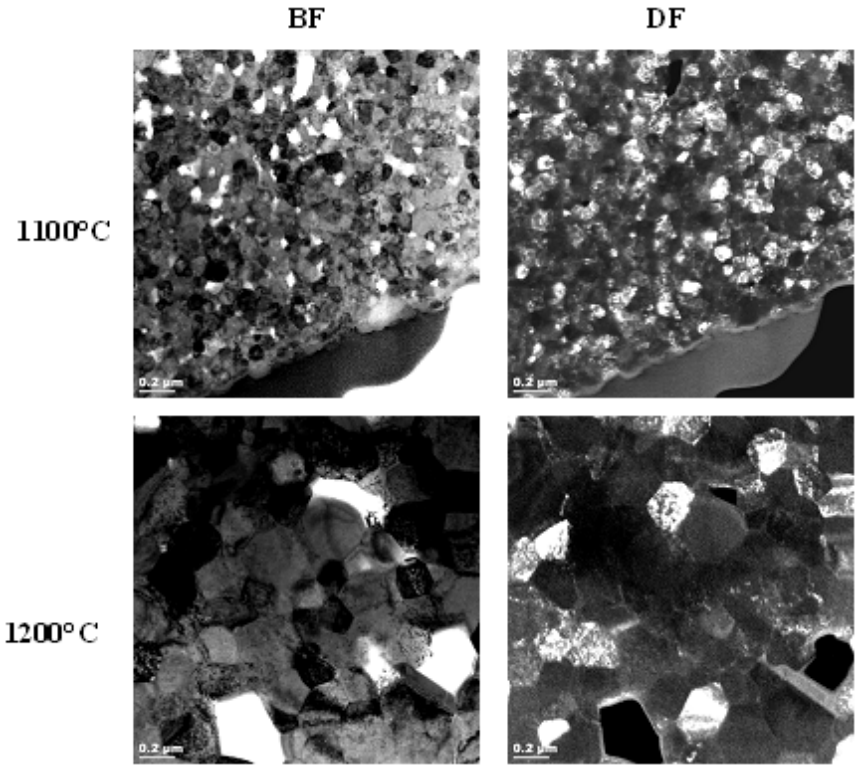

Fig. 5. TEM images for samarium doped ceria (SDC). Bright Field (BF), Dark Field (DF) and Selected Area Diffraction (SADP).

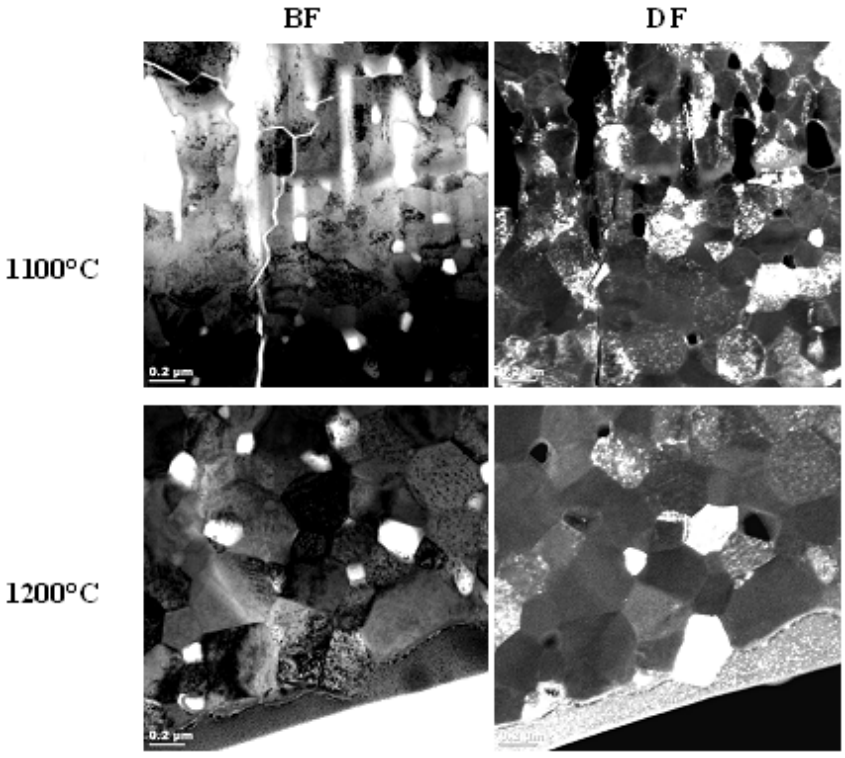

Fig. 6. TEM images for ytterbium doped ceria (YDC). Bright Field (BF), Dark Field (DF) and Selected Area Diffraction (SADP).

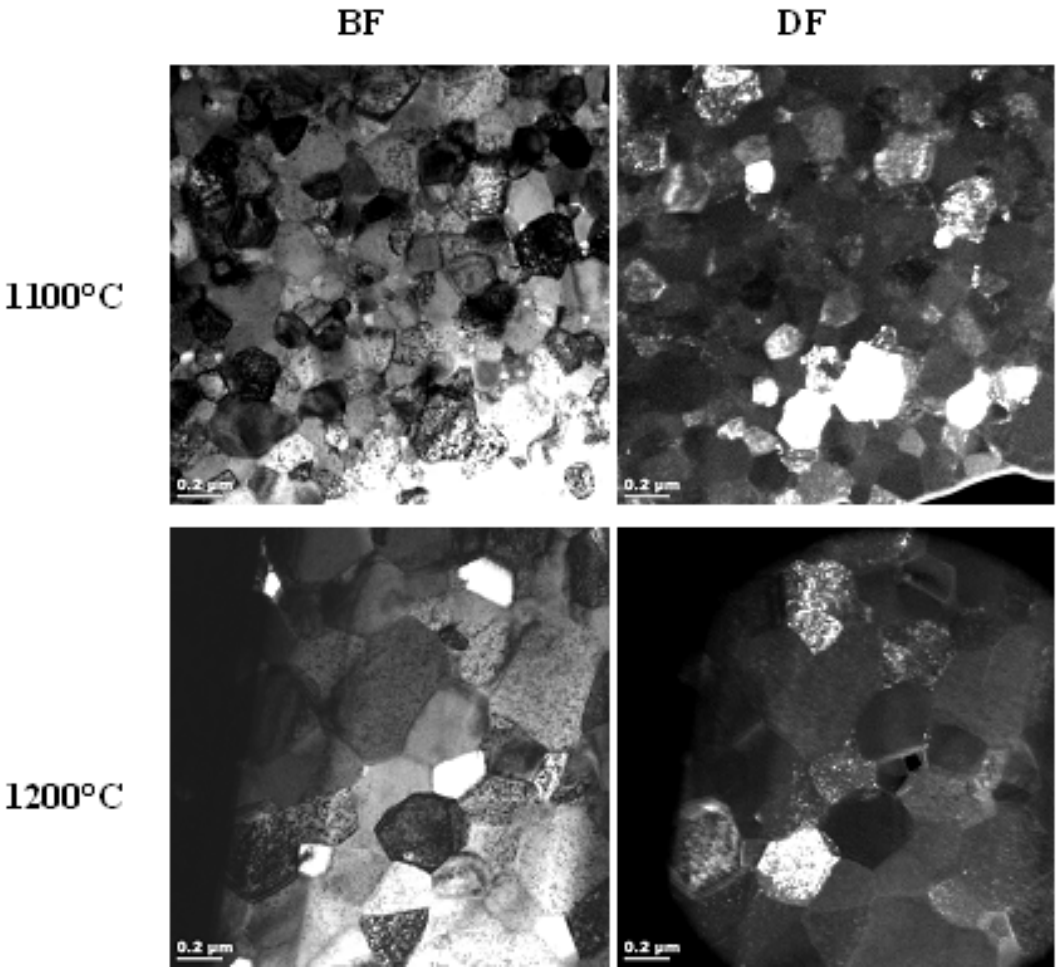

Fig. 7. TEM images for gadolinium doped ceria (GDC). Bright Field (BF), Dark Field (DF) and Selected Area Diffraction (SADP).

For comparison SPS sintering of the same samples at 1200°C was performed and the samples were subsequently analyzed by TEM and SEM. The results indicated that increasing the maximum sintering temperature from 1100°C to 1200°C significantly influences the final grain size of the samples. Thus, the grain sizes of bulk SPS sintered samples at 1200 °C showed a two fold increase compared to the data obtained for the same samples SPS sintered at 1100°C (Table 1). Moreover, the increase in grain size in case of Gd^{3+} doped ceria (GDP) sintered at 1200°C was so significant that the SADP of the GDC coarse structure was distinct. Figure 6 shows that the diffraction pattern of GDC has discrete reflections rather than the well distributed powder pattern associated with the fine structure in the other samples.

Table 1. Microstructural and conductivity data for all SPS sintered M^{3+}/CeO_2 samples.

Sample (Sinter Temperature)	Mean powder particle size (± 3 nm)	Mean sintered particle size (± 5 nm)	High Frequency E_a (±0.03 eV)	Low Frequency E_a (±0.03 eV)
SDC (1100)	26.4	80	0.81	1.02
YDC (1100)	19.3	94	1.10	1.17
GDC (1100)	31.4	160	0.95	1.03
SDC (1200)	26.4	214	1.20	1.09
YDC (1200)	19.3	185	1.17	1.05
GDC (1200)	31.4	609	0.97	0.85

HRTEM images of Yb^{3+} doped ceria (YDC) and Sm^{3+} doped ceria (SDC) samples sintered at 1100 ^{o}C were recorded. Figure 8 shows images of grain boundaries for the YDC and SDC. The grains didn't contain any amorphous or secondary phases. On the other hand, the crystalline area contains extended defect. The ledges shown in Figure 7b are growth-related defects, which were mostly observed in grains containing (111) planes. Examination of the grain boundaries did not show evidence of grain boundary-localized precipitate formation. The lack of detectable grain boundary or bulk precipitates is consistent with prior work and may contribute to enhanced ionic conductivity [27].

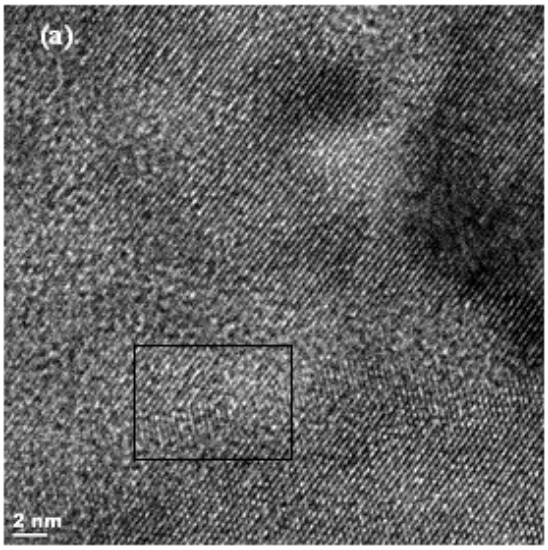

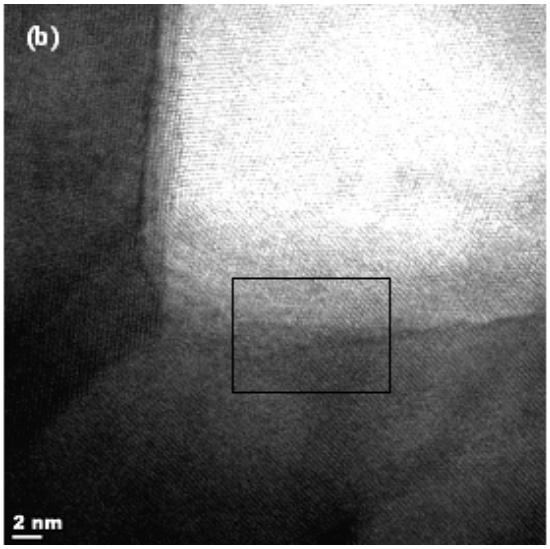

Fig. 8. HREM images of precipitate-free grain boundaries in M^{3+}-doped ceria, YDC (a) and SDC (b), sintered at 1100 ^{o}C.

AC impedance measurements of the SPS-sintered M^{3+}-doped ceria samples were performed at 250°C and 290°C. In each case, two depressed arcs were observed corresponding to bulk, grain boundary and electrode/ electrolyte interface. The first high frequency arc was associated with conductivity derived from the bulk (grain interior) and grain boundary conductivity owing to the high frequency less than 1 MHz. The second low frequency arc was assigned to the impedance associated with the electrode/electrolyte interface that corresponds to oxygen ionic conduction. For all samples, both the low high frequency arcs decreased significantly when increasing the temperature. This shows that the grain boundary resistance decreases with the increase in temperature. The total resistivity values of the samples were determined from the low-frequency intercept on the real axis in the impedance spectrum. The impedance of GDC sintered at 1200°C and SDC sintered at 1100°C show a partly blocking behavior, which indicates that oxygen ions are the dominating mobile species since electrons or protons would result into a non-blocking behavior. From our SEM results (Figure 3) we found that GDC displays the largest percentage of grain growth upon SPS sintering. Usually, in the case of nanosized materials, the space charge field is negligible, while in materials with larger grain sizes, a high temperature treatment activated ion movement to reduce space charge. In the case of GDC we can speculate that the conductivity behavior was close to the lower limits in grain size for this effect to produce.

According to the Arrhenius law, the dc conductivity is related to activation energy as follows

$$\sigma = \sigma_0 EXP(\frac{-Ea}{K_B T})$$

where σ is the dc conductivity, σ_0 is the pre-exponent constant, Ea is the activation energy, K_B is Boltzmann's constant, and T is absolute temperature. The curve can be fitted linearly. The corresponding activation energies can be obtained from the slope. The activation energy for the oxygen ion migration of M^{3+} doped ceria was determined from the low frequency impedance. The values were registered in the range of 0.85-1.17eV range, which is in agreement with values reported in literature [12]. The high frequency Arrhenius plots indicated the electron-hole conductivity increased with increasing temperature. The activation energy for the electron-hole migration were in the range of 0.81-1.20 eV, which is similar to the value of oxygen ion migration. The lowest activation energy at high and low frequencies was observed for the SDC which was sintered at 1100°C (Table 1). GDC sintering 1100°C displayed the highest ionic conductivity in the low frequency regime. This effect may be due to high relative ionic conductivity of grain boundaries parallel to the applied field. The strong increase in total conductivity of the gadolinium doped sample with respect to grain size as well as its good conductivity at low sintering temperatures makes this an attractive material for future work.

4. Conclusions

Nanometric powders of ceria doped with 20 at% of three different rare earth metals (Sm, Gd, Yb) were synthesized by a solution method and subsequently sintered by SPS at 1100 and 1200°C. The particle sizes of the precursor powders were 26.4 (SDC), 19.3 (YDC) and 31.4 nm (GDC), respectively. The grain sizes of the samples SPS sintered at 1100°C registered a three to five fold increase relative to the precursor powders. When the SPS sintering temperature was increased to 1200°C, the grain growth was enhanced to an 8-19 fold increase relative to the precursor powder. The SPS sintered samples had a typical ceria cubic crystal structure and a low compact porosity. Electrical impedance data of the samples show that the impedance of all the samples decreased with increasing temperature, and that the grain size and the sintering temperature have important to their impedance. The activation energy values for the oxygen ion migration are in the range of 0.85-1.17eV, while the activation energy values for the electron-hole migration were in the range of 0.81-1.20 eV. GDC sintered by SPS at 1100°C displayed the highest ionic conductivity, which makes it an attractive material for future work.

References

[1] B. Butz, P. Kruse, H. Stromer, D. Gerthsen, A. Muller, A. Weber, E. Ivers-Tiffe, Solid State Ionics **176**, 3275 (2007).
[2] M. Martin, Electrotransport and demixing in oxides. Solid State Ionics **136-137**, 331(2000).
[3] S. Kim, J.S.Lee, C. Mitterbauer, Q.M. Ramasse, M C. Sarahan, N.D. Browning, H. J. Park, Chem.Mater. **21**, 1182-1186 (2009).
[4] T. Hosomi, M. Matsudad, M. Miyake, J. Eur. Ceram. Soc. **27**, 173(2007).
[5] Z. Shao, S. M. Haile, Nature **431**, 170 (2004).
[6] B. C. H. Steele, Solid State Ionics **129**, 95(2000).
[7] A. E. C. Plsmqvist, M. Wirde, U. Gelius, M. Muhammed, Nanostructured Mater. **11**, 995 (1999).
[8] T.H.Etsell, S.N.Flengas Chem. Rev. **70**, 339(1970).
[9] H.Inaba, H.Tagawa, Solid State Ionics **83**, 1(1996).
[10] B.C.H. Steele, J.A.K. Zheng, J. Bae, Proceedings of the second international conference on ceramics in energy applications (Institute of Energy, London, 1994), pp. 109.
[11] S. Kim, J. Maier, J. Eur. Ceram. Soc. **24**, 1919(2004).
[12] A. Tschope, S. Kilassonia, R. Birringer,Solid State Ionics **173**, 57(2004).
[13] A. Tschope, E. Sommer, R. Birringer, Grain, Solid State Ionics **139**, 255 (2001).
[14] A. Tschope, Solid State Ionics **139**, 267 (2001).
[15] A. Tschope, C. Bauerle, R. Birringer, J. Appl. Phys. **95**, 1203 (2004).
[16] S. Kim, J. Fleig, J. Maier, Phys. Chem. Chem. Phys. **5,** 2268(2003).
[17] S. Kim., J. Maier, J. Electrochem. Soc. **149**, J73(2002).
[18] S. Kim, U. Anselmi-Tamburini, H. J. Park, M. Martin, Z. A. Munir, Adv. Materials **20**, 556 (2008).
[19] Y. M. Chiang, E. B. Lavik, I. Kosacki, H. L. Tuller, J. Y. Ying, Appl. Phys. Lett. **69**,185 (1996).
[20] U. Anselmi-Tamburini, F. Maglia, G. Chiodelli, A. Tacca, G. Spinolo, P. Riello, S. Bucella, Z. A. Munir: Adv. Functional Mat. **16**, 2363(2006).
[21] S. Wang, H. Inaba, H.Tagawa, T. Hashimoto, J. Electrochem. Soc. **144**, 4076(1997).
[22] N. Maffei, A.K. Kuriakose, Solid State Ionics **107**, 67(1998).
[23] I. Riess, D. Braunshtein, D.S. Tannhause, J. Am. Ceram. Soc. **64**, 479(1981).
[24] M. Pechini, Method of preparing lead and alkaline earth titanates and niobates and coating method using the same to form a capacitor. US Patent 3330697(1967).
[25] K. Yamashita, K. V. Ramanujachary, M. Greenblatt, Solid State Ionics **81**, 53 (1995).
[26] G. F. Taylor, Apparatus for sintering refractory material such as in the manufacture of cemented carbides. US 2022528 (1935).
[27] K. Inoue, Electric-discharge sintering. US Patent No. 3241956(1966).
[28] G. Petot-Ervas, C. Petot, D. Zientara, J. Kusinski, Materials Chemistry and Physics **81**,305 (2003).
[29] S.W. Wang, L.D. Chen, T. Hirai, J .Mater. Res. **15**, 982 (2000).
[30] J. R. Groza, A. Zavaliangos, Materials Science & Engineering, A: Structural Materials: Properties, Microstructure and Processing **A287**(2), 171 (2000).
[31] L. A. Stanciu, J.R. Groza, V. Y. Kodash, M. Crisan, M. Zaharescu**.** Journal of the American Ceramic Society **84**(5), 983 (2001)
[32] R. S. Mishra, A.K. Mukherjee. Materials Science&Engineering A: Structural Materials: Properties, Microstructure&Processing A **287**(2) 178 (2000).

*Corresponding author: carmenplapcianu@yahoo.com; carmen@infim.ro